December 1, 1987

Electric field and plasmadensity measurements in the strongly-driven daytime equatorial electrojet: 1. The unstablelayer and gradient drift waves

R. F. Pfaff
M. C. Kelley
E. Kudeki
Bela G. Fejer, *Utah State University*
K. D. Baker

JOURNAL OF GEOPHYSICAL RESEARCH, VOL. 92, NO. A12, PAGES 13,578–13,596, DECEMBER 1, 1987

Electric Field and Plasma Density Measurements in the Strongly Driven Daytime Equatorial Electrojet
1. The Unstable Layer and Gradient Drift Waves

R. F. PFAFF,[1] M. C. KELLEY,[2] E. KUDEKI,[3] B. G. FEJER,[4] AND K. D. BAKER[4]

Electric field and plasma density instrumentation on board a sounding rocket launched from Punta Lobos, Peru, detected intense electrostatic waves indicative of plasma instabilities in the daytime equatorial electrojet. Simultaneous measurements taken by the Jicamarca radar showed strong 3-m type 1 electrojet echoes as well as evidence of kilometer scale horizontally propagating waves. The in situ electric field wave spectra displayed three markedly different height regions within the unstable layer: (1) a two-stream region on the topside between 103 and 111 km where the electron current was considered to be strongest, (2) a gradient drift region between 90 and 106.5 km where the upward directed, zero-order electron density gradient was unstable, and (3) an "interaction" region between 103 and 106.5 km where both of these instabilities were linearly unstable. The unstable altitudes and differentiation showed good agreement with the simultaneous 3-m Jicamarca backscatter radar observations. In the region where the density gradient was unstable, large-amplitude waves with large scale sizes (wavelengths of roughly 1–2 km) were observed. These kilometer scale waves dominated the observed in situ spectrum despite the fact that the peak in the linear gradient drift growth rate occurred at wavelengths of only a few hundred meters. Comparisons of the measured δE and $\delta n/n$ components of the large-scale waves verify the basic process inherent to the gradient drift instability: density enhancements were observed coincident with westward electric fields, and density depletions were associated with eastward fields. The amplitudes (10–15 mV/m) of these horizontal waves were strong enough to drive vertical two-stream secondary waves. In the region where these waves existed and the electrojet current was strongest, evidence of wave steepening was seen, and the resulting waveforms of the large structures displayed a "flat-topped" nature. In the lower region of the electrojet the irregularity power occurred over a broad range of wavelengths, estimated to be in the range of tens of meters to kilometers, and fell off rapidly for the shorter wavelengths. Throughout the gradient drift region, shorter-scale waves often occurred in bursts which appeared controlled by the larger electric field structures.

1. INTRODUCTION

Equatorial E region plasma instabilities and waves have been studied for decades with ground-based and in situ techniques and have also been the subject of intense theoretical research and numerical studies (see the review by *Fejer and Kelley* [1980]).

The linear plasma instabilities in the equatorial electrojet are basically classified according to two types: the collisional two-stream and the gradient drift instability, although the unstable oscillations both emerge from a single dispersion relation [*Rogister and D'Angelo*, 1970; *Sudan et al.*, 1973; *Fejer et al.*, 1975]. The two-stream instability is a fast process, in which meter scale waves are created initially in a linearly unstable cone defined where the components of the relative electron-ion drift velocity exceed roughly the ion acoustic speed [*Farley*, 1963; *Buneman*, 1963]. By contrast, the gradient drift mechanism is a relatively slowly developing instability in which longer-wavelength structures are generated whenever the ambient electric field has a component parallel to the gradient in the local electron number density [*Simon*, 1963; *Maeda et al.*, 1963]. Although linear theory accounts quite well for the generation of the ionospheric irregularities, observations of these waves depict characteristics that depart considerably from the first-order predictions. For example, the very existence of waves propagating perpendicular to the electrojet current, as observed by backscatter radars, implies that the electron flow is no longer laminar but has evolved into a more complex, turbulent like layer. The present status of the observations and theory of the electrojet instabilities has recently been reviewed by *Farley* [1985].

The most systematic experimental work on electrojet irregularities has been provided by observations made with coherent backscatter radars, for which the principal results have been obtained at 50 MHz at the Jicamarca Radio Observatory in Peru. Such backscatter radar observations and their theoretical implications have been reviewed by *Farley* [1979, 1985] and are also discussed in the first companion paper in this series [*Kudeki et al.*, this issue].

In situ studies of the electrojet irregularities at the dip equator have been carried out exclusively with probes on sounding rockets flown along westward trajectories launched from either Thumba, India (dip angle, 0.5°S), or from Punta Lobos, Peru (dip angle, 0.5°N). The majority of the early irregularity experiments were conducted using Langmuir probes which provide electron number density and $\delta n/n$ (fluctuation) measurements [e.g., *Prakash et al.*, 1972; *Smith and Røyrvik*, 1985]. These observations, taken in both the daytime and nighttime electrojets, have shown the relationship of the irregularity layers to the gradients in the ambient electron number density profile and have provided information concerning the wave amplitudes as a function of estimates of their scale sizes.

[1]Laboratory for Extraterrestrial Physics, NASA Goddard Space Flight Center, Greenbelt, Maryland.
[2]School of Electrical Engineering, Cornell University, Ithaca, New York.
[3]Aeronomy Laboratory, University of Illinois, Urbana.
[4]Center for Atmospheric and Space Sciences, Utah State University, Logan.

Paper number 7A9028.
0148-0227/87/007A-9028$05.00

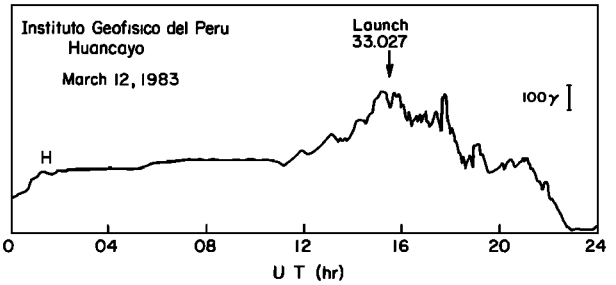

Fig. 1. Magnetometer observations at the Huancayo Observatory for March 12, 1983, showing the presence of a strong electrojet current during the time of launch. Subtract 5 hours from UT for local time.

Electric field detectors using the double-probe technique have also been flown at the dip equator, although the only dc results showing the vertical (polarization) electric field have been those reported by *Sartiel* [1977]. *Sampath and Sastry* [1979] investigated wave electric fields on two noontime flights with low apogees (117 km and 128 km) and one early morning flight with a slightly higher apogee (140 km) launched from Thumba, India. (The two midday flights were actually the same as those analyzed by *Sartiel* [1977].) This analysis revealed electric field wave components associated with the gradient drift instability between 85 and 105 km, with the largest-amplitude signals occurring near the lowest rocket frame frequencies.

Pfaff et al. [1985] compared data from three different daytime rocket flights flown from Punta Lobos, Peru, including wave electric field observations gathered during both strong and mild electrojet experiments conducted at midday, and plasma density fluctuation observations obtained during weak electrojet conditions in the late afternoon. They showed that waves were present only in the regions predicted to be linearly unstable for the combined two-stream and gradient drift instabilities. The data for the strong electrojet case presented by *Pfaff et al.* [1985] will be analyzed in considerably greater detail in this paper.

Recently, *Prakash and Pal* [1985] reported simultaneous measurements by double-probe electric field detectors and Langmuir probes on two rockets flown in the daytime electrojet in India during the presence of type 1 VHF backscatter radar echoes. These experiments showed large-amplitude ($\sim$10 mV/m) electric fields in the horizontal direction between 95 and 105 km which were attributed to the gradient drift mechanism. They estimated the predominant wavelengths of these structures to be roughly 0.5–1.0 km, although these values would be altered if the dispersive nature of the waves and the effect of the neutral wind were considered, as we discuss below.

This paper is one in a series of papers discussing results from the Condor electrojet experiments conducted during March 1983 from Punta Lobos, Peru. The first paper in this series [*Kudeki et al.*, this issue], hereafter referred to as paper 1, describes the campaign objectives and discusses the radar results for both daytime and nighttime electroject conditions. The next two papers both present rocket measurements made during the daytime electrojet experiment. This paper (paper 2) presents an overview of the in situ observations followed by an examination of the measured long-wavelength waves characteristic of the gradient drift instability. Then, in paper 3 [*Pfaff et al.*, this issue], detailed in situ observations of the two-stream waves are presented, and their theoretical implications are discussed. Tantamount to the interpretations and results in papers 2 and 3 are the simultaneous radar observations and discussion presented in paper 1.

An outline of the present paper is as follows: A brief summary of the geophysical conditions and ground-based observations is given in section 2 followed by a description of the rocket instrumentation and pertinent payload dynamics in section 3. The data presentation constitutes section 4, followed by a discussion (section 5) of the observations in terms of both linear and nonlinear theoretical ideas. In section 6 the main conclusions of this paper are presented.

2. Geophysical Conditions and Ground-Based Observations

On the morning of March 12, 1983, a large magnetic deflection was observed by the ground-based magnetometer at the Huancayo Geophysical Observatory in Peru. As shown in Figure 1, this magnetic perturbation indicates that a strong midday electrojet current was flowing overhead. When an estimate of the nonionospheric ΔH component is subtracted, this current is seen to create a ΔH excursion of roughly 140 γ during the time of the rocket flight. In addition, a sporadic E layer was observed on ionograms recorded at Huancayo during this time, providing evidence of density irregularities in the E region overhead [see *Pfaff et al.*, 1985].

As discussed in paper 1, during this period the large vertically pointing array at the Jicamarca Radio Observatory detected 3-m backscatter echoes between the altitudes of 93.5 and 112.75 km, with vertically propagating type 1 echoes (two-stream waves) confined to a narrower layer of roughly 4 km width centered around 104 km. As well, the radar observed the presence of kilometer scale waves propagating in the east-west direction with an average horizontal phase velocity of 125 m/s, prior to the neutral wind correction, and with an average dominant wavelength of roughly 2–2.5 km.

Backscatter observations were also obtained at Jicamarca from a small steerable antenna that also showed strong 3-m type 1 echoes. These data, which were sampled at a range corresponding to a 56° angle measured from vertical toward magnetic west, displayed "saturated" type 1 phase velocities at values of roughly 315 m/s. By comparing the observed Doppler shift of type 1 waves from the steerable antenna with that from the vertical spectra obtained with the main Jicamarca antenna [*Balsley et al.*, 1976] and assuming spatial homogeneity, the neutral wind velocity was estimated to be roughly 80 m/s eastward, as shown in paper 1. Thus the average phase velocity of the large-scale waves derived from the Jicamarca interferometer data was roughly 205 m/s westward in the neutral wind frame. As we shall see, the phase velocity and neutral wind measurements carried out at Jicamarca are crucial to fully understanding the in situ wave data.

3. Rocket Instrumentation and Flight Parameters

The Cornell University electrojet experiment (rocket 33.027) consisted of a 14-inch-diameter payload equipped with three sets of 5.5-m tip-to-tip stacer booms, as shown in Figure 2. Spherical sensors extended by these booms comprised double-probe detectors configured to measure the dc and wave electric field components and fixed-bias Langmuir probes which measured the relative electron density and plasma fluctuations. The nose cone was fitted with an absolute plasma

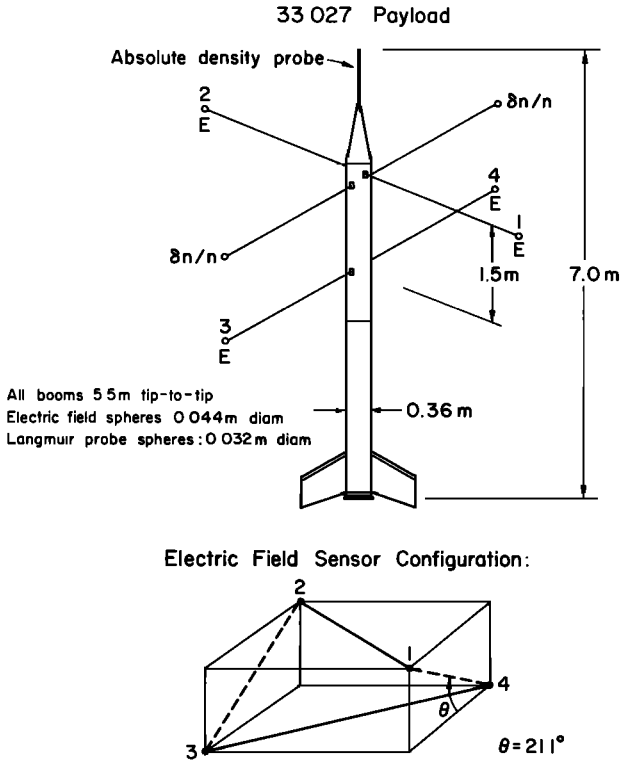

Fig. 2. Sketch of payload sensor configuration drawn to scale for rocket 33.027, including the attached second-stage motor. The geometry of the electric field sensors depicting the four measured components is shown in the lower portion.

density probe built at the Utah State University [*Baker et al.*, 1985].

With the physical phenomena described above in evidence, Taurus-Orion sounding rocket 33.027 was launched at 1034:36 LT on March 12, 1983, from Punta Lobos, Peru. The locations of the launch site and ground-based observing stations are shown in Figure 3. The payload followed a trajectory directed along the model dip equator, with an essentially constant horizontal velocity component of 482 m/s in the direction of geomagnetic west.

The rocket reached an apogee of 128 km at a flight time of 181 s. Throughout the data-taking portion of the flight, the rocket attitude was oriented with a 9.3° coning half angle centered within a degree of the vertical direction. Thus as the rocket precessed, the spin plane containing the electric field booms was always oriented to about 10° of the horizontal magnetic field plane.

4. Data Presentation

Overview of the Wave Data and Ambient Plasma Parameters

General characteristics. A summary presentation of the data taken during the rocket's upleg traversal through the electrojet region is shown in Plate 1. On the right-hand side, power spectra from a frequency-time sonogram (shown later) have been mapped into equally spaced altitude bins to create a frequency-height sonogram. Plotted on the left-hand side is the simultaneously measured electron density profile from the Langmuir probe instrument which has been normalized to the plasma frequency probe data [*Baker et al.*, 1985]. As is clear in the sonogram, the rocket encountered a distinct region of irregularities between 90 and 111 km, which displayed further differentiation within the layer. In the upper portion of the electrojet a well-defined region of high-frequency oscillations was observed. Notice that a very strong spectral feature at roughly 70 Hz, embedded in this region, appeared exactly where the electron density gradient changed sign at 106.5 km and then shifted in a smooth manner to lower frequencies at slightly higher altitudes. In paper 3 we will discuss this feature in detail and argue that it represented the strongest spectral component of the primary two-stream spectrum.

The majority of the spectral wave energy between 90 and

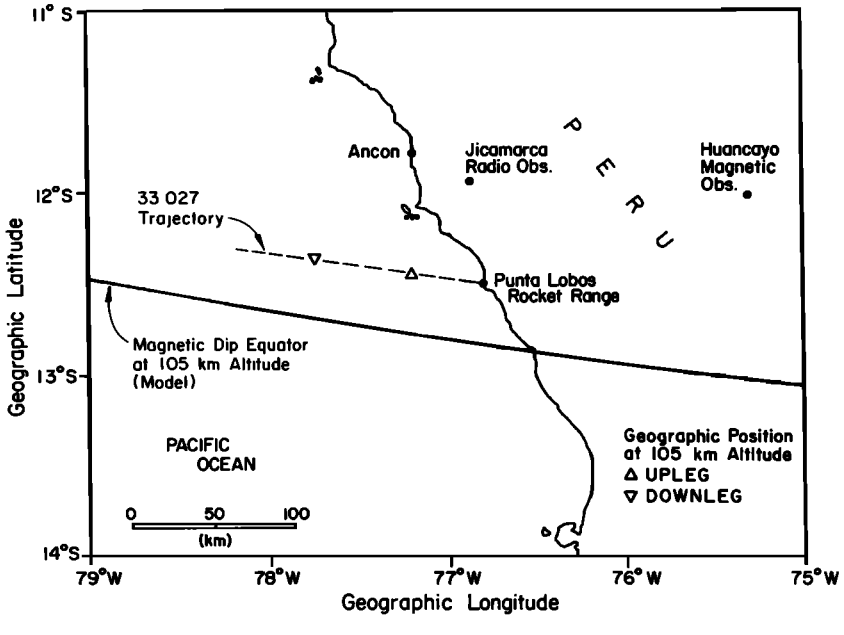

Fig. 3. Trajectory of rocket 33.027, the model magnetic dip equator at 105 km altitude, and locations of the ground-based observing stations.

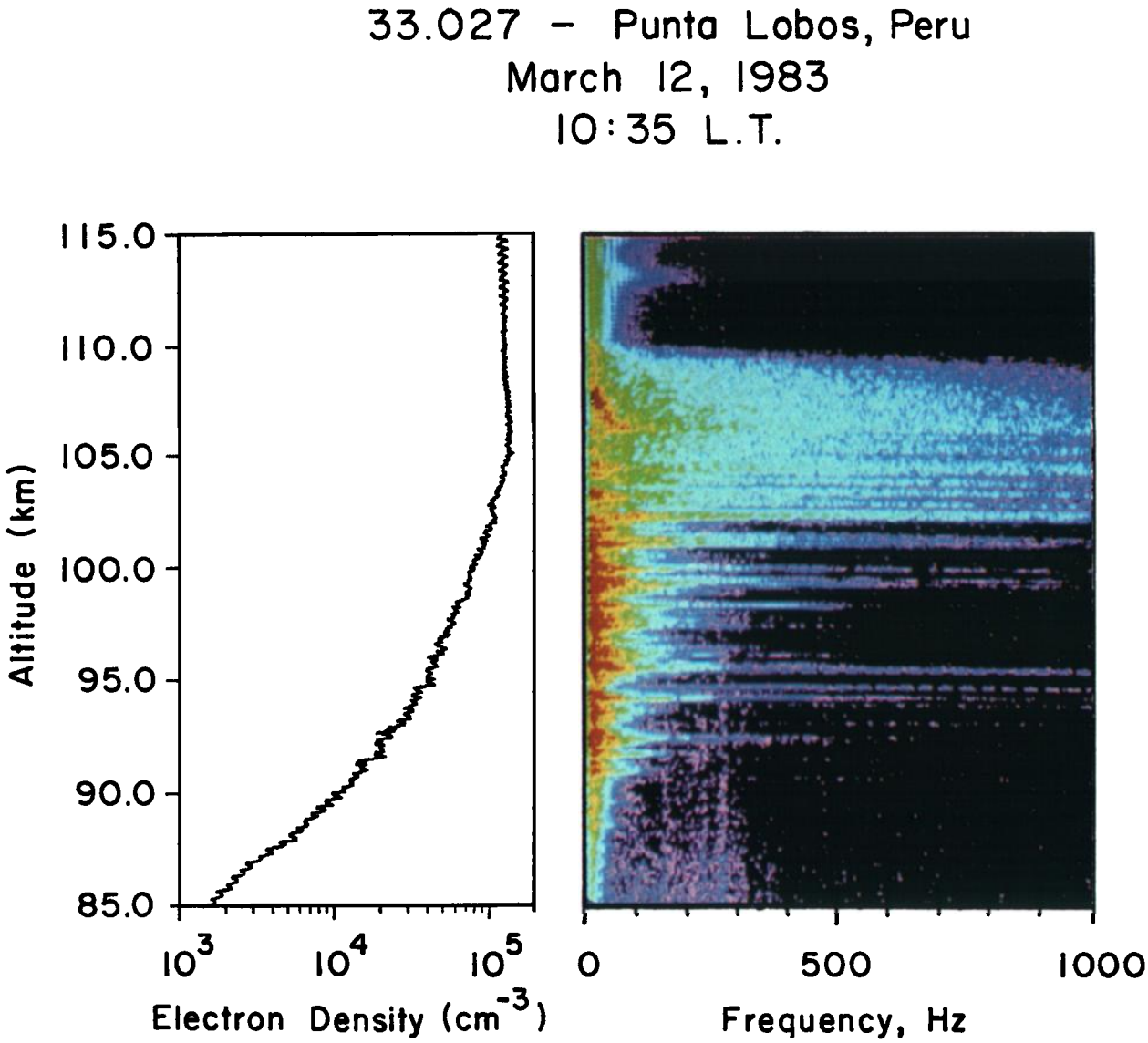

Plate 1. Measured plasma density profile and frequency-height sonogram of the electric field wave data observed on the upleg. The color levels in the sonogram encompass over 40 dB in power, with red denoting stronger amplitudes than blue.

103 km occurred well below 100 Hz in the rocket frame. This region was associated with the upward (unstable) gradient in electron density. These waves will be interpreted as being part of the broad spectrum of irregularities driven by the gradient drift process. The largest amplitudes occurred at the longest wavelengths which can be seen directly as enhancements and depletions in the electron density profile in Plate 1, as well as in the horizontal dc-coupled electric field data discussed below.

Another presentation of the electric field data is shown in Figure 4 for both the upleg (Figure 4*a*) and downleg (Figure 4*b*) traversals of the electrojet region. The top panels display 0- to 1-kHz, frequency-time sonograms computed from one component of the electric field data. Notice that the overall dimensions of the irregularity characteristics of the unstable layer were similar on both the upleg and downleg, which were spaced approximately 68 km apart in horizontal range. In both traversals the same distinct high-frequency layer of waves was detected on the topside, with fluctuations primarily at lower frequencies beneath this layer.

Below the sonograms in Figures 4*a* and 4*b* the horizontal components of the dc-coupled electric field measurements are shown. These spin plane fields corresponded very nearly to the full strength of the horizontal electric fields in geomagnetic coordinates, since the rocket axis was tipped only 10° from the vertical. Notice that the horizontal electric field strengths on the upleg and downleg had peak values of the order of 10–15 mV/m and were strong enough to drive both secondary two-stream and gradient drift vertically propagating waves. These east-west electric fields depict long-period wave structures, indicative of kilometer scale horizontal waves.

A portion of the electric field wave power evident in the sonograms, obtained by integrating the spectrum over the frequency range 16–100 Hz, is also shown in Figures 4*a* and 4*b*. The projected length of the electric field detector along the magnetic equator, which varied sinusoidally with the rocket's spin, is shown in the bottom panel. The power profiles show that the waves were modulated at twice the spin rate throughout the entire irregularity region. Analysis of the observed modulation shows that the wave power peaked whenever the component of the electric field probe in the plane perpendicular to the magnetic field was maximum. Since $\mathbf{E} \times \mathbf{k} = 0$ for an electrostatic wave, this indicates that the waves propagated predominantly in this plane, as expected for electroject irregularities.

Notice also the strong irregular modulation of the electric field waves in the sonograms and in the 16- to 100-Hz power plots, particularly in the lower portion of the electrojet. Qualitatively, this modulation correlated with changes in the east-west dc-coupled horizontal electric fields and implies that the large structures controlled the shorter-scale (in this case, higher-frequency) waves.

The important point that we wish to make in this section is that the distinct irregularity layers observed within the electrojet region displayed very different characteristics in different altitude intervals. We will show in this paper why this distinction existed and will demonstrate how the spectral features of the observed waves depended on the local characteristics of the electron density profile, the electron drift velocity, and the large-scale wave electric fields.

Electron density and current profiles. The smoothed ambient electron number density profile measured on the upleg is shown in Figure 5*a*. In this presentation, data from the plasma frequency probe were used above 97 km [*Baker et al.*, 1985] and were extended by the normalized Langmuir probe data below this height. The electron density increased with altitude with a gradient scale length of roughly 10 km at 103 km and reached a maximum value of 1.3×10^5 cm^{-3} at 106.5 km. Above this peak the gradient was small and slightly negative. The observed values depict a typical midday electron density profile at the equator [cf. *Aikin and Blumle*, 1968, Figure 4]. Note that the large fluctuations in electron density, characteristic of the large-scale structures, have been suppressed in this presentation, using averaging and interpolation techniques.

Although a direct measurement of the electron current density is not available, an estimate of this value can be inferred from the measure of the intensity of the overhead current by the ground-based magnetometer at Huancayo (see Figure 1) in the following manner. *Richmond* [1973] showed that the current strength from several in situ measurements off the coast of Peru correlated well with the ground-based magnetometer ΔH deflection. Thus we have taken the average measured current profile compiled by *Richmond* [1973] and scaled it to the Huancayo ΔH deviation of about 140 γ (above the background) measured during this flight. The resulting current density profile is shown in Figure 5*a*. A maximum current of 11.5 A/km^2 was found for this model profile at 108 km.

The third key plasma parameter in the electrojet region pertains to the electron-neutral collision frequency ν_e and the ion-neutral collision frequency ν_i. These changing parameters are incorporated in the variable $\psi = \nu_e \nu_i / \Omega_e \Omega_i$, which is also plotted in Figure 5*a*, where Ω_e and Ω_i are the electron and ion gyrofrequencies. The collision frequencies were calculated using the expressions in the work by *Forbes* [1981]. This curve shows the rapid increase of the collision frequencies below about 100 km.

From the profiles shown in Figure 5*a* we can infer the electron drift speed, the polarization electric field, and, using linear theory, an estimate of the horizontal phase velocity of the medium and short-scale (100 m $> \lambda >$ 10 m) electrojet instabilities. The plasma drift velocity $\mathbf{V}_d$ may be computed using the relationship

$$\mathbf{V}_d = \mathbf{V}_i - \mathbf{V}_e = \mathbf{J}/qN_e \tag{1}$$

where $\mathbf{V}_i$ and $\mathbf{V}_e$ are the ion and electron drift velocities, $\mathbf{J}$ is the current density, and q is the electronic charge. We assume $N_e = N_i$. The resulting drift velocity profile using (1) is presented in Figure 5*b*. Assuming that the ions were at rest, this calculation implies that the maximum electron drift speed was 520 m/s westward and occurred at 108 km. For the magnetic field strength in Peru at this altitude, the polarization electric field corresponding to an $\mathbf{E} \times \mathbf{B}$ drift velocity of this magnitude yields a value of 13.5 mV/m directed upward.

Linear phase velocity and frequency/wave number conversion. The theoretical phase velocity of the linear, small-amplitude medium- and short-wavelength gradient drift and two-stream waves traveling parallel to the plasma drift direction is given by

$$V_\phi = \omega/k = V_d/(1 + \psi) \tag{2}$$

where k is the wave number parallel to the plasma drift and ω is the oscillation frequency measured in the neutral frame. The phase velocity using the model drift velocity calculated above is plotted in Figure 5*b*.

The fluid threshold of the two-stream instability occurs

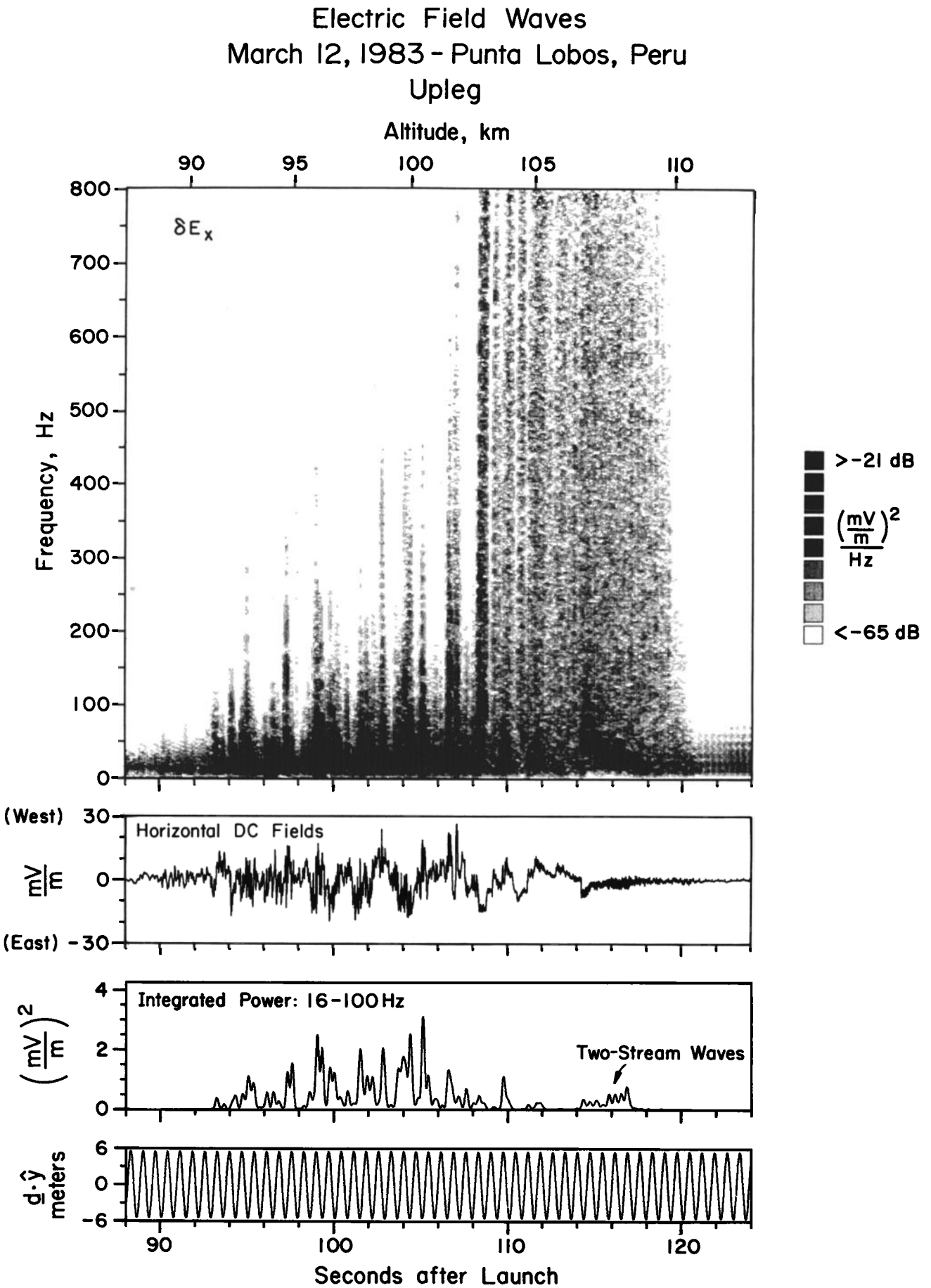

Fig. 4a. Data from the electric field instrument for the upleg traversal of the rocket through the electrojet region.

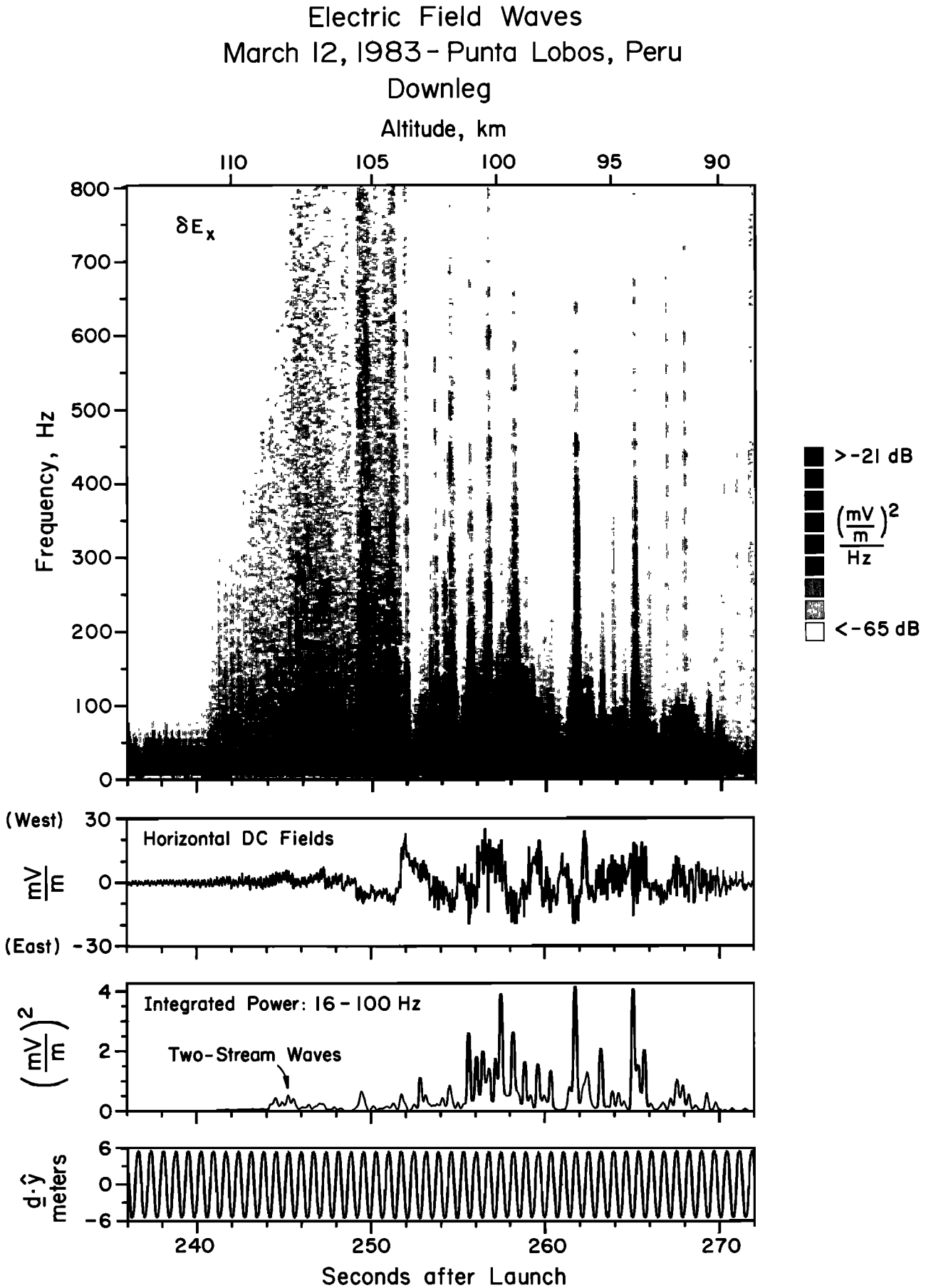

Fig. 4*b*. Data from the electric field instrument for the downleg traversal of the rocket through the electrojet region.

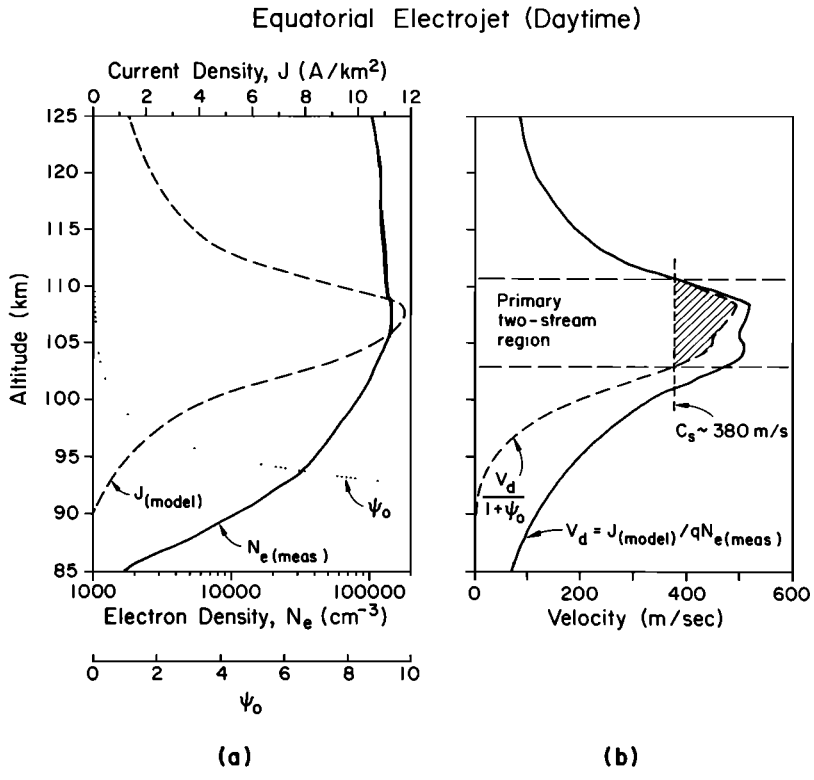

Fig. 5. (*a*) Ambient plasma parameters measured or inferred during the flight of rocket 33.027. (*b*) Electron drift profile calculated using the measured absolute density and the model current profile. The horizontal instability phase velocities computed using the linear fluid dispersion relation are shown by the dashed line labeled $V_d/1 + \psi_0$.

where $V_d/(1 + \psi)$ exceeds the local ion acoustic velocity C_s. An approximate value for this parameter is indicated in Figure 5*b*, inferred from the vertical Jicamarca type 1 phase velocities (see paper 1). Notice that in the height range of 103–110 km the model phase velocity clearly exceeded the estimated acoustic velocity. Although T_e may have varied somewhat with altitude, particularly if wave heating occurred (see paper 3), this height interval is in excellent agreement with that of the observed layer of high-frequency oscillations, which we associate with the two-stream instability. This agreement thus lends credence to our first-order electron drift profile and phase velocity calculations.

The model phase velocity can be used as a rough guide for converting observed frequency to wavelength which will be useful in interpreting the wave observations. In this regard, the observed frequency of a wave in the rocket frame is related to the Earth-fixed reference frame wavelength via the Doppler shift relation:

$$\omega_{\text{obs}} = \mathbf{k} \cdot \mathbf{V}_R - \mathbf{k} \cdot \mathbf{V}_\phi - \mathbf{k} \cdot \mathbf{U}_N \tag{3}$$

where $\mathbf{V}_R$ is the rocket velocity, $\mathbf{V}_\phi$ is the phase velocity (which is always parallel to $\mathbf{k}$), and $\mathbf{U}_N$ is the neutral wind velocity. The measured horizontal component of $\mathbf{V}_R$ projected along the model magnetic equator was 482 m/s throughout the flight. Thus equation (3) shows that as $\mathbf{V}_\phi$ and $\mathbf{U}_N$ changed within the unstable layer, a given horizontal wavelength would correspond to several different observed frequencies in the rocket frame. For this particular experiment, in the region where the waves were propagating fastest, they were Doppler-shifted to very low rocket frame frequencies, since the combined rocket and neutral wind velocity in the direction of the waves was comparable to that of the fastest waves. Of course, the wave vectors were not all oriented in the horizontal direction and possessed a significant distribution of phase velocities, but this equation provides a starting point for associating wavelengths with the observed rocket frame frequencies. A detailed discussion of this relationship for propagating electrostatic turbulence may be found in the work by *Pfaff* [1986].

Observations of Large-Scale Waves

The region of the positive, zero-order vertical electron density gradient was the seat of both the longest-wavelength irregularities and the largest-amplitude electric field fluctuations observed in the electrojet. We investigate these long-wavelength waves first by studying their appearance in the dc-coupled horizontal electric field data and then by relating these fields to the observed perturbations in electron density.

Horizontal electric field measurements. The presence of large-scale waves in the equatorial electrojet can be seen in the raw data of the two perpendicular spin plane dc-coupled electric field channels, plotted in the lower panels of Figure 6 for the upleg traversal of the electrojet. The potential differences measured between the sensors have been divided by the fixed tip-to-tip electrode distances in this presentation. The prime indicates that these were the rocket frame fields.

Using the rocket attitude, trajectory information, and a model of the magnetic field, the $\mathbf{V} \times \mathbf{B}$ fields due to the vehicle motion through the Earth's magnetic field have been calculated for the same period of the flight and are shown in the upper panels of Figure 6. The smooth $\mathbf{V} \times \mathbf{B}$ envelopes represent the expected measured fields had there been no geophysical electric fields present. The strong modulation evident in

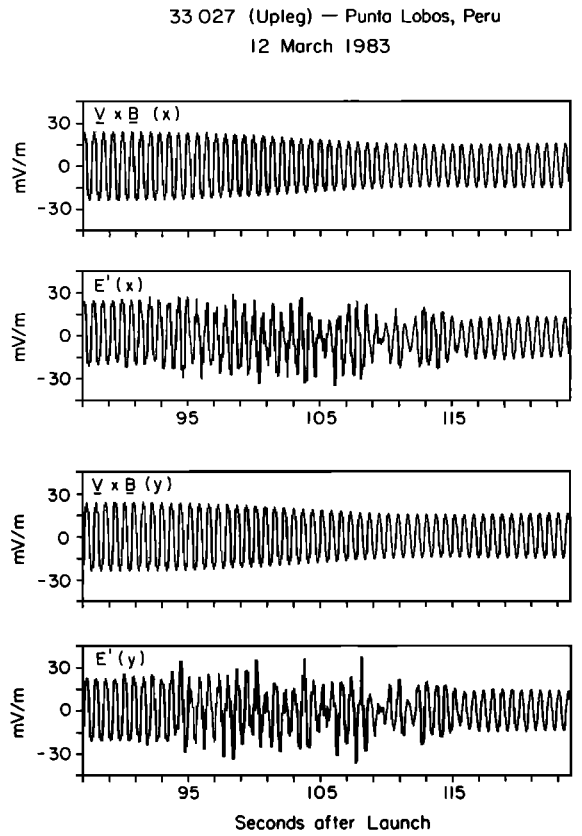

Fig. 6. Measured electric fields (lower panels) and computed **V** × **B** fields (upper panels) corresponding to the two orthogonal spin plane components on the upleg traversal of the electrojet. The modulation in the raw data is due to the electric fields of the electrojet irregularities.

the measured fields indicates that large-scale irregularities were present in the electrojet. Outside the region of the large perturbation fields, note that the amplitude and phase of the measured fields and the calculated **V** × **B** fields match nicely. This is to be expected, since the ambient zonal electric field component at the equator is generally quite small, less than 1 mV/m.

For this study, the only reliable dc-coupled electric field components available were from the two orthogonal spin plane detectors, since the axial component $E'(z)$ suffered a severe and varying dc offset and thus precluded our measuring the vertical electric field in the electrojet. However, in regard to the horizontal fields, since the rocket axis was tipped from the magnetic zenith by a coning half angle of only 10°, the missing third component, $E'(z)$, contained only a very small contribution from these fields. Therefore the two spin plane components, $E'(x)$ and $E'(y)$, can be used to adequately describe the horizontal geophysical electric fields. Because of this small tilt, however, the vertical electric field also contributed to the spin plane components but probably only altered the derived horizontal fields by at most a few millivolts per meter near the region of the strongest current.

In order to deduce the geophysical horizontal fields, the **V** × **B** values were subtracted from the rocket frame measurements shown in Figure 6, and then the resulting components were rotated into geomagnetic coordinates, as shown in Figure 7. Notice immediately that the measured horizontal electric fields were primarily in the geomagnetic east-west direction, and that the wave electric fields at times exceeded 10 mV/m. Although the existence of some finite $k_{\parallel}$ cannot be ruled out, the small fluctuations seen in the magnetic north-south direction (∥ **B**) were probably in a large part due to inaccuracies in matching the observed **V** × **B** fields with the calculated model fields and other noiselike errors in the measurement. Contributions of this order would also be expected in the east-west fields as well. The longer time-varying component seen in the north-south fields which occurred at the coning frequency of the rocket represents, to a large degree, the error invoked by not including the axial $E'(z)$ component in the computation.

Extensive analysis [*Pfaff*, 1986] of the vector wave fields using the third, axial electric field component showed that these long-wavelength irregularities contained no significant component in the vertical direction. Thus we conclude that the large-scale waves detected in situ represented primarily one-dimensional propagation along the magnetic equator. This result is consistent with other in situ observations of horizontally polarized large-scale waves reported by *Prakash and Pal* [1985], and with the Jicamarca radar observations reported in paper 1.

Large-scale structures in the ambient electron density. If the large-scale electric field oscillations were indeed due to the gradient drift instability, they should have associated fluctuations in the electron density. These perturbations can be readily seen in the electron density profile in Plate 1. In order to analyze these structures, a zero-order electron density profile was fit to the data (as shown in Figure 5*a*) and then was subtracted from the "raw" profile. By dividing by the local zero-order density, a $\delta n/n$ value was found. This procedure was carried out using the data from each of the two electron density instruments on the rocket: the plasma frequency probe

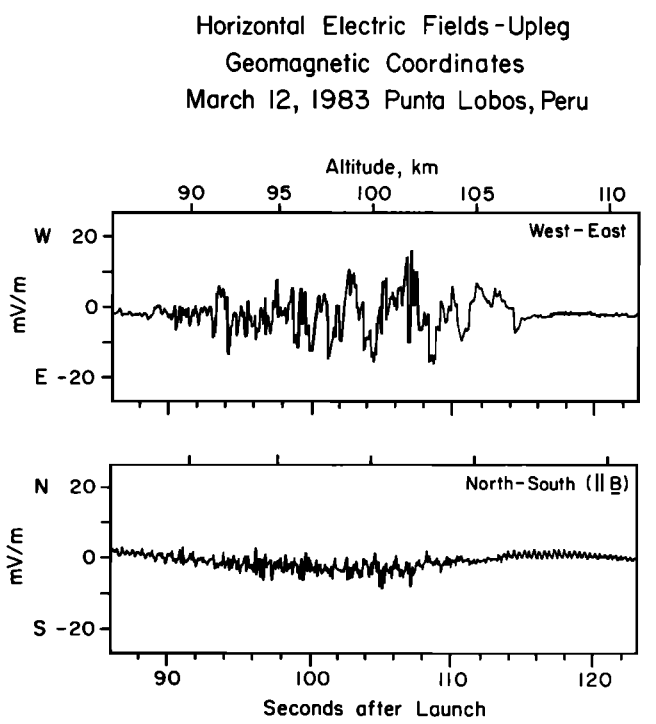

Fig. 7. Measured horizontal electric fields in geomagnetic coordinates for the upleg traversal of the rocket through the electrojet. The high-frequency wave components have been filtered from these data in this presentation.

and the fixed-bias Langmuir probe. (Note that the plasma frequency probe did not "lock on" until the rocket was above about 97 km altitude.) The results for the two instruments are shown in the bottom two panels of Figure 8. For comparison, the top panel shows the east-west electric fields computed above. (The arrows in the bottom panel will be referred to below.)

Notice that both sets of $\delta n/n$ computations from the independent instruments show wave structure which correlates well not only with each other but also with the electric field data. (The downleg data, not shown, also revealed similar results.) The large electric field excursion near 112 s on the upleg does not seem to be matched in the $\delta n/n$ data, but since this was the region of the "nose" in the density profile, possibly part of the density wave crest was subtracted as part of the "ambient" profile, thus diminishing the $\delta n/n$ value for that portion of the data.

The largest electron density enhancements and depletions were clearly of the order of 10% of the background plasma density. It is not clear why the amplitudes of the two density probes were not the same. This issue has been discussed in detail by *Baker et al.* [1985]. The plasma frequency probe data were more reliable, since that instrument does not depend on vehicle potential or on several other factors that affect Langmuir probes.

Phase velocity and wavelength determination. The dominant period of the large-scale waves can be estimated from their time series representations shown in Figure 8. The arrows in the bottom panel point to periodic maxima in the electron density structure in the Langmuir probe data from which the dominant period appears to have been approximately 4.5 s. A similar dominant period was present in the downleg data. For a first-order analysis we assume that these waves traveled at a roughly constant average phase velocity (at least throughout the middle portion of the layer) and that this velocity was that measured simultaneously by the Jicamarca interferometer (roughly 125 m/s in the Earth-fixed frame) as shown in paper 1. Thus, using (3) and including the 80-m/s eastward neutral wind measured at Jicamarca, the dominant wavelength corresponding to a rocket frame period of 4.5 s was approximately 1.6 km, in reasonable agreement with the average Jicamarca-derived wavelength of a few kilometers reported in paper 1.

The appearance of structures with periods roughly half as long is also suggested in the data, particularly in the lower electrojet. The Jicamarca observations report that the phase velocities of the large-scale waves fell off rapidly with decreasing altitude (see paper 1). It is difficult to estimate the wavelength of the in situ oscillations without a recognizable periodic structure in the waveform and a reliable profile of the neutral wind velocity versus height. For reference, a horizontal wave with an in situ period of 2 s and a phase velocity of 100 m/s in the neutral wind frame would correspond to a wavelength of about 925 m in the presence of an 80-m/s eastward neutral wind and a wavelength of about 750 m in the absence of a neutral wind. These wavelengths were near or below the lower limit of horizontal scale lengths discernable by the Jicamarca interferometer. Spectral analysis of the in situ data which suggests that structures did exist with wavelengths of several hundreds of meters, is presented later on.

Analysis of the large-scale waveforms. Before leaving the discussion of the large-scale waves, we wish to comment on the detailed shapes of their waveforms. Another presentation

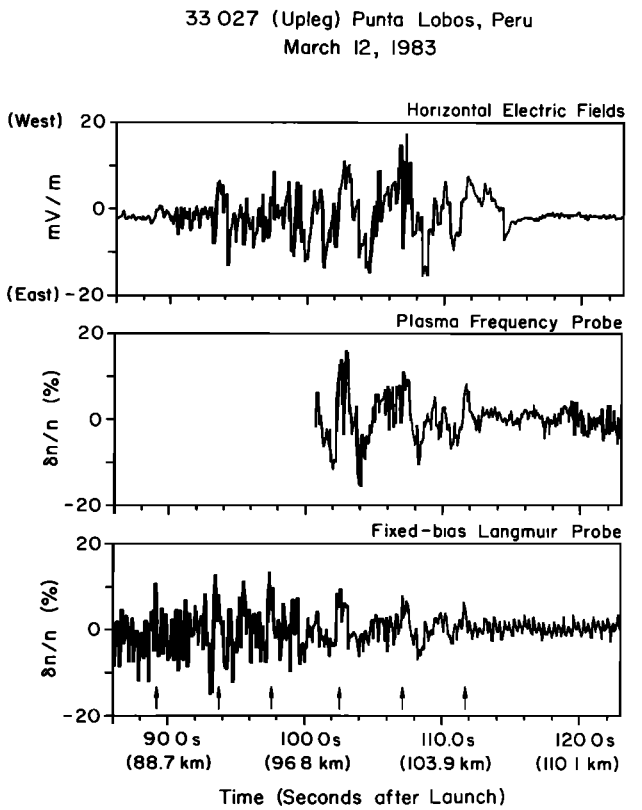

Fig. 8. Comparison of the enhancements and depletions observed in the two independent electron density instruments (bottom panels) with the measured horizontal electric fields (top panel) for the upleg.

of the upleg east-west electric fields is shown in Figure 9, computed using the sum of the squares of the orthogonal electric field measurements. The applicability of this technique to these data is discussed in the appendix. As can be seen here and also in the downleg data shown earlier in Figure 4*b*, the dc-coupled electric fields corresponding to the region of strong electrojet current (near 105 km) displayed sharper waveforms than did those at the lower altitudes, where their form had a somewhat "noisier" yet quasi-sinusoidal nature. In fact, the enlarged presentation of the fields near 104–105 km shown in the lower panel in Figure 9 depicts "square" or flat-topped waveforms, suggesting that the amplitudes of the large-scale waves were saturated by some geophysical process. In no instance were any of the electric field components, from which these waveforms were computed, clipped or limited by instrumental effects.

The actual steepening of the waveforms is somewhat difficult to parameterize because of the combination of the westward launch and the dispersive nature of the large-scale waves in which longer-wavelength waves propagate more slowly. Because the horizontal rocket velocity component was in the same direction and greater than that of the waves, slightly shorter, yet faster waves may have been Doppler-shifted to the same rocket frame frequencies as those of the longer, slower waves depending on the particular combinations of $\mathbf{k} \cdot \mathbf{V}$ in the rocket frame. This same effect would distort the waveforms in the time domain. It is unlikely, however, that this created the square shapes, although it may have slightly altered the true shapes, square or otherwise, of some of the waveforms.

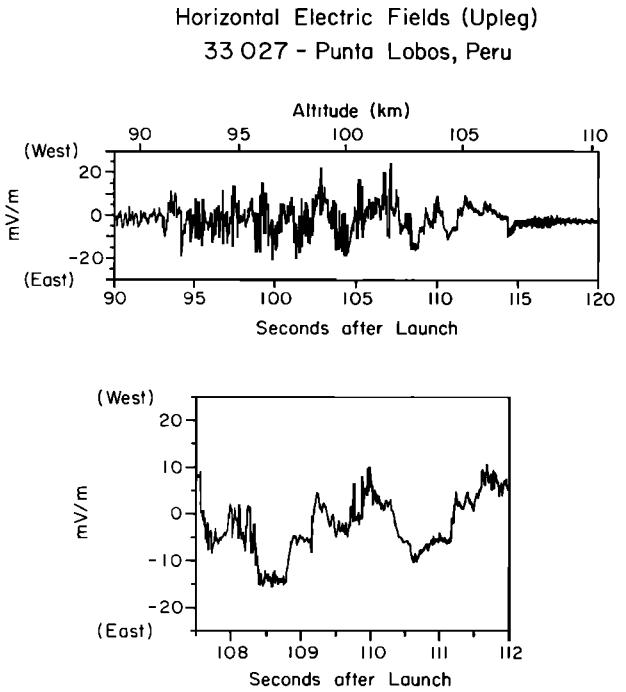

Fig. 9. Another representation of the horizontal electric fields observed during the upleg traversal of the electrojet. In the lower panel the enlarged waveform shows the steepened, "flat-topped" nature of the fields in the region where the current was strongest.

Spectral Analysis of the Gradient Drift Waves

In the lower portion of the electrojet layer (< 100 km) the waves principally represent gradient drift driven irregularities with very small phase velocities. The observed irregularities displayed an absence of a steady high-frequency component, as seen in the sonograms shown earlier in Plate 1 and Figures 4*a* and 4*b*. A detailed examination reveals a "bursty" nature for the wave data in the lower region that appeared related to the largest excursions in the dc electric field (see the sonograms and power profiles in Figures 4*a* and 4*b*). Other observations of "burstiness" of low-frequency waves in the electrojet have been reported previously by *Prakash et al.* [1972].

In order to parameterize the spectral characteristics of the long- and medium-wavelength gradient drift waves, we must consider relatively long time series, in which a sufficient number of the lower-frequency wave periods are present. Because of the vertical motion of the rocket, however, several of the plasma and wave parameters (e.g., ψ, $\mathbf{U}_N$, $\mathbf{V}_\phi$, angular distribution of $\mathbf{k}$) may have changed considerably in the region represented in one power spectrum, essentially violating the stationarity requirements necessary to interpret the spectral features. We have examined power spectra covering several different time scales and present representative spectra of approximately 8 s duration which each correspond to an altitude interval of roughly 6–7 km (which is effectively somewhat smaller if the influence of the Hanning window used in the analysis is considered). Although much of the microstructure of the waves is smeared out, these computations enable general conclusions about the nature of the irregularities in the lower electrojet to be drawn.

Spectra of the gradient drift oscillations in the lower electrojet region for the upleg and downleg are shown in Figure 10 together with the spin plane electric field time series from which these computations were made. Notice the enhancements at low frequencies, such as those seen at roughly 1 Hz. In general, the appearance of a peak in power spectra of electrostatic spatial waves implies the existence of a wave packet propagating primarily in one direction. For horizontally propagating waves these Doppler-shifted oscillations near 1 Hz probably corresponded to wavelengths of about 500 m. Similar peaks with estimated scale lengths of several hundred meters observed in the equatorial electrojet were reported by *Pfaff et al.* [1982].

The power spectra shown in Figure 10 level off between roughly 2 and 20 Hz. For horizontally propagating waves with near-zero phase velocities, this frequency band would correspond to wavelengths of approximately 30–300 m, in the presence of an eastward neutral wind of 80 m/s, and roughly 25–250 m without the neutral wind component. Notice that the spectra display sharp drops in power at higher frequencies. To parameterize this, we have modeled the spectral densities with power laws. The measured spectral indices in Figure 10 were approximately -1.2 between 2 and 20 Hz and approximately -4.5 between 40 and 80 Hz. (The latter interval roughly corresponds to horizontal wavelengths between 5 and 15 m.) The "break" at around 30 Hz was probably due to where the growth rate tapered off for the shorter-scale waves (see section 5) but also may have been emphasized by the superimposed artificial spectral knee of k^{-2} in electric field data that occurs for scale lengths less than roughly twice the double-probe component in the direction of propagation (i.e., ≤ 11 m for $\mathbf{k} \parallel \mathbf{d}$.) This effect is discussed in more detail in paper 3. Despite the unknown spatial attenuation factor, the important result shown in these spectra and also displayed earlier in the sonograms is that the wave power for the shorter scales (higher frequencies) appeared severely diminished in the lower electrojet on both the upleg and downleg.

In the above analysis the observed oscillations were interpreted as horizontally propagating waves. Some fraction of the waves encountered in this region, however, were undoubtedly propagating in oblique and vertical directions as well. Although the electric field detector was most sensitive to horizontal electric field components, it also detected "off-axis" waves with amplitudes decreased essentially by the cosine of the angle between the wave vector and the double-probe direction. Such vertical and oblique waves would undergo different vehicle Doppler shifts than for the horizontal waves, contributing to the power spectral densities at both high and low rocket frame frequencies, as given by (3). Not knowing the angular distribution of the irregularities as a function of wave number (even in a statistical sense) that were encountered by the rocket probes limits our analysis. We feel fairly confident, however, of the general results stated above.

Summary of the Observations

Below, we summarize the most important results from the in situ electrojet observations described above.

1. The unstable electrojet layer was highly differntiated with respect to altitude and was composed of three different regions: a two-stream region of high-frequency waves on the topside between 103 and 111 km, where the electron current was considered to be strongest; a gradient drift region between 90 and 106.5 km, where the upward directed electron density gradient was unstable; and an "interaction" region between 103 and 106.5 km, where both the two-stream and gradient drift instabilities were linearly unstable.

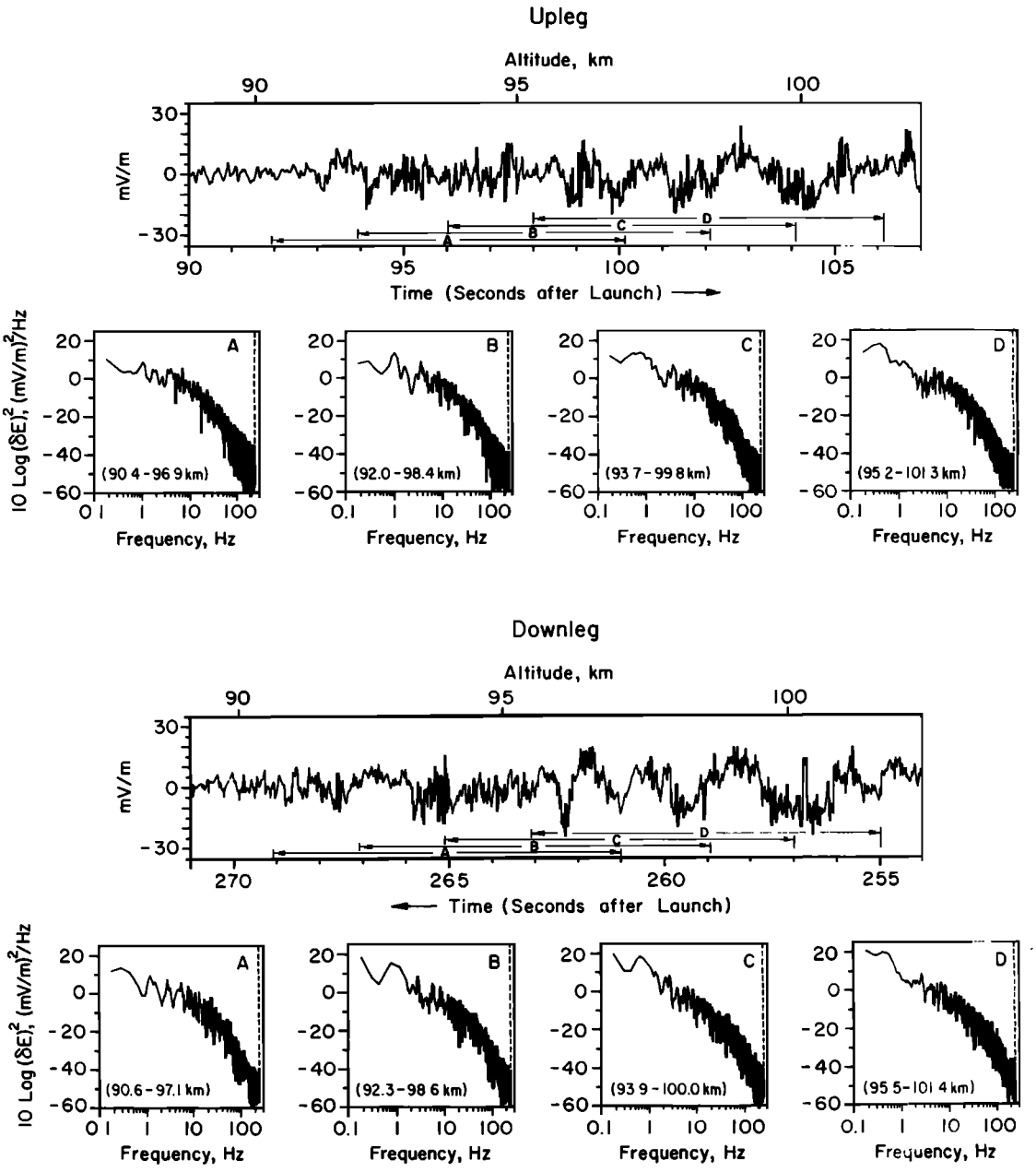

Fig. 10. Low-frequency electric field spectra from the lower electrojet (gradient drift region) for the upleg and downleg. The spectra were computed from the total spin plane (horizontal) component of δE. The letter designations for each spectrum correspond to the intervals in the time series presentations in the upper panels. The dashed line at 242 Hz represents the receiver 3-dB low-pass filter.

2. The unstable altitudes and observed irregularity characteristics within the layer showed good agreement with the Jicamarca vertical backscatter echoes (see paper 1).

3. The observed electric field irregularities displayed a twice-per-spin modulation throughout the layer, which for the payload and boom geometry in this experiment indicated that the waves were oriented in the plane perpendicular to the magnetic field.

4. Large-amplitude, long-wavelength waves were observed by both the electric field and plasma density detectors in the region of the positive (destabilizing) gradient in electron density between 92 and 106 km on both the upleg and the downleg.

5. The largest observed modes had wavelengths of roughly 1.6 km (using the Jicamarca phase velocity) and were observed to propagate primarily in the east-west direction. These waves had electric field amplitudes that were 10–15 mV/m and density fluctuations that were roughly 10%.

6. In general, the δE and $\delta n/n$ components of the large-scale waves were observed to be in phase; i.e., density enhancements (depletions) were observed coincident with westward (eastward) electric fields.

7. The shape of the large-scale waveforms included sharp, steepened edges and a "flat-topped" or square wave appearance in the upper part of the gradient drift region (103–106 km) in both the upleg and downleg data.

8. The data displayed a "bursty" nature for the relatively short scale irregularities throughout the region of the large-

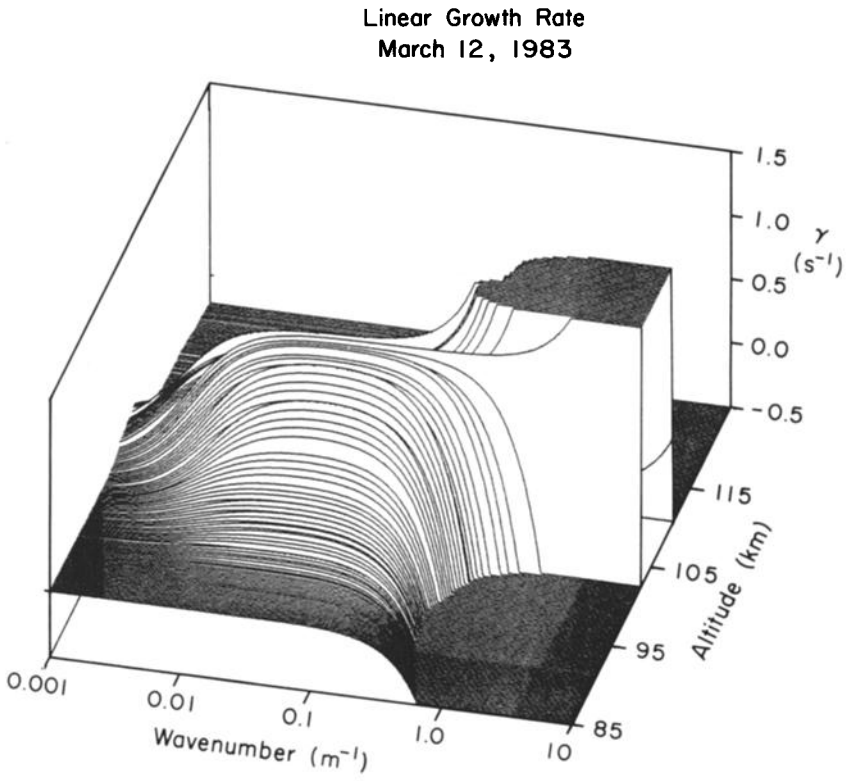

Fig. 11. Three-dimensional representation showing the computed linear growth rate for the combined two-stream and gradient drift instabilities, using the same parameters as those plotted in Figure 5*a*.

scale waves, including the lower region of the equatorial electrojet. The modulation of the shorter-scale waves appeared to be related to the larger-scale electric field structures.

9. In the lower region of the electrojet, most of the observed wave power occurred at the lowest rocket frame frequencies and, in general, corresponded to wavelengths of tens of meters to kilometers. The power decreased with increasing observed frequency and fell off sharply for shorter wavelengths in this region.

5. Discussion

The Unstable Layer: Linear Growth Rate Predictions

To begin the analysis of the observed electrojet irregularity layer, the unstable wave number domain is computed from the linear fluid theory. These computations establish benchmarks against which to compare the observations and with which to ascertain where nonlinear processes are needed to interpret the data. A three-dimensional representation of the growth rate γ versus wave number k versus height is given in Figure 11, computed from the standard linear expression for electrojet instabilities for waves perpendicular to the magnetic field [e.g., *Fejer et al.*, 1975]:

$$\gamma \simeq \frac{\psi}{\nu_i(1+\psi)}(\omega_k{}^2 - k^2C_s{}^2) + \frac{\omega_k k_0}{k} - 2\alpha N_0 \tag{4}$$

where

$$k_0 = \frac{\nu_i}{\Omega_i}\frac{1}{(1+\psi)}\frac{1}{L_N} \tag{5}$$

Here α is recombination coefficient, L_N is the gradient scale length given by $N(\partial Z/\partial N)$, and the other variables are defined as before. The generalized real part of the oscillation frequency, including long-wavelength modes (i.e., without the assumption that $\omega \gg \gamma$), is [*Kudeki et al.*, 1982]

$$\omega_k = \frac{\mathbf{k}\cdot\mathbf{V}_d}{(1+\psi)[1+(k_0/k)^2]} \tag{6}$$

The growth rates shown in Figure 11 were computed using the measured electron density profile, the model electron current profile, and the parameter ψ, as plotted in Figure 5*a*. Other representations of these growth rates are discussed by *Pfaff et al.* [1985].

As seen in Figure 11, the primary two-stream region is depicted by the large growth rates at the highest wave numbers between 103 and 110 km, whereas the primary gradient drift region corresponds to the broad range of longer-wavelength waves below 106.5 km. Between 103 and 106.5 km, both the two-stream and gradient processes are linearly unstable.

In the two-stream region, since the most unstable wavelengths are of the order of the ion mean free path and shorter, the fluid computations are not valid, and kinetic expressions must be used instead [*Farley*, 1963; *Schmidt and Gary*, 1973]. Nevertheless, the fluid theory is useful for predicting the threshold altitudes and the general unstable wavelength domain of the irregularities. Notice the excellent agreement between the observed layer of high-frequency oscillations between 103 and 111 km (see Plate 1 and Figures 4*a* and 4*b*) and the predicted unstable two-stream region. The growth rates for the long-wavelength waves above 106.5 km where the ambient density gradient changes sign are damped by the stabilizing gradient term and by the recombination term. In actu-

ality, the data also show this long-wavelength cutoff in the upper portion of the layer, but because of the severe Doppler shift (see paper 3) this cannot be seen in the sonogram presentations.

Most of the observed high-frequency waves in the interaction region (103–106.5 km) are actually produced by secondary two-stream waves, as discussed in paper 3. However, since the localized plasma drifts due to the large-scale wave electric fields are of the same order as those due to the horizontal current, agreement between the one-dimensional model computations and the observed waves appears somewhat better than is probably the case. This illustrates how the simple model used in computing (4) is limited, particularly since the driving current was undoubtedly modulated by the large-scale waves in this region, a factor which was not included in these calculations.

In the gradient drift region below 103 km, notice that the growth function peaks at wavelengths of a few hundred meters in Figure 11 and is damped (i.e., $\gamma < 0$) at both a high and a low "crossover" wave number. The low wave number cutoff (and hence the peak) results from using the complete expression for the oscillation frequency (6) and thus is a consequence of the long-wavelength theory where $\omega \sim \gamma$. The computed linear growth curves also show how energy is not simply injected at one particular point in the gradient drift spectrum but rather is input throughout a whole range of wave numbers. This range is broadest where L_N is large. As with the two-stream region, the unstable growth rate computations predict fairly well the altitude regime where the gradient drift irregularities were observed in the unstable layer.

Large-Scale Horizontally Propagating Waves

Introduction. The large-amplitude, kilometer scale waves observed in this experiment were detected in the region where the electron density gradient was destabilizing. This is in accordance with a gradient drift explanation for their generation, since the daytime polarization electric field is also directed upward. This conclusion agrees with similar daytime in situ observations reported earlier [e.g., *Prakash et al.*, 1972; *Pfaff et al.*, 1982; *Prakash and Pal*, 1985]. In this section we concentrate on the large-scale modes and then, in the next section, consider the gradient drift spectrum as a whole.

Kilometer scale electrojet irregularities were discussed qualitatively by *Balsley and Farley* [1973] and by *Farley et al.* [1978], and then more rigorously by *Kudeki et al.* [1982, 1985] and *Kudeki* [1983], who explained them (and their reduced phase velocities) in terms of the linear gradient drift theory for $\omega \sim \gamma$. The simultaneous observations of the east-west electric fields and the plasma density waveforms reported here (see Figure 8) showed that large enhancements and depletions of the plasma number density were associated with respective downward and upward plasma perturbation velocities, corresponding to westward and eastward wave electric fields, respectively. The observations are of fundamental importance, since they illustrate and confirm the basic gradient drift instability process. We now wish to discuss these enhancements and depletions as an unstable mode, with a characteristic phase velocity and wavelength.

Phase velocity and wavelength. The general phase velocity of gradient drift waves propagating parallel to the drift velocity follows immediately from (6) such that

$$V_\phi = \frac{\omega}{k} = \frac{V_d}{(1 + \psi)[1 + (k_0/k)^2]} \tag{7}$$

As discussed by *Kudeki et al.* [1982], the phase velocity is dispersive for small k values and equals one-half its short-wavelength value for $k = k_0$.

As shown in paper 1, during the time of launch, the average Jicamarca-derived phase velocity for the large-scale waves at 105 km was roughly 205 m/s in the neutral wind frame. Assuming that this velocity corresponded to a mode given by $k \sim k_0$, using (7) and a value of ψ of 0.22, the electron drift velocity would then be of the order of 500 m/s. This value is in good agreement with the model electron drift velocity profile computed in Figure 5*b* and lends credence to the ambient polarization field of approximately 13.5 mV/m, which was inferred from the model electron drift velocity. It also supports the use of the 80-m/s eastward neutral wind value included in the phase velocity determination.

As discussed in section 4, using the Jicamarca phase velocity, the dominant in situ period of the large-scale waves corresponded to a wavelength of approximately 1.6 km, in reasonable agreement with the average Jicamarca measured wavelength of 2–2.5 km. For the moment, let us assume that the dominant mode observed by both the rocket and the radar corresponded to k_0. Since k_0 is a function of the ambient electron density gradient L_N, we can use the density measurements to check the consistency of our computations and assumptions. At 105 km the in situ measured electron gradient scale length was about 10 km, which corresponded to a wavelength of 2.7 km (using (5)). A scale length of 8 km (observed at 100 km altitude) would correspond to a dominant wavelength of 2.2 km. These values, which are in reasonable agreement with both the in situ and radar-derived wavelengths, appear to support a relationship between the dominant mode of the daytime gradient drift spectrum with that given by (5).

Despite the agreement between the measured k_{dominant} and k_0, however, the relationship between these values may be fortuitous, and the actual explanation for the observed peak may actually involve a different set of criteria. For example, in the nighttime electrojet the density gradients are sharper and more jagged, but the measured wavelengths on the average are longer, of the order of 4–5 km [*Kudeki et al.*, 1982; *Kudeki*, 1983], despite the fact that the values of k_0 associated with these density gradients would correspond to shorter scales. At night the observed dominant mode may occur at longer wavelengths because of the reduced damping effect of the recombination term. Further, if $k_{\text{dominant}} < k_0$, this would be consistent with the lower observed nighttime phase velocities using (7), although smaller electron drift velocities may also account for the lower nighttime phase velocities. Another possibility is that the dominant wavelength is determined by the overall dimensions of the irregularity layer, which are narrow during the daytime and enlarged at night.

The extent to which the large-scale waves "filled out" the unstable gradient region can be studied to some degree with the in situ data, although the inability to distinguish between changes in wavelength and phase velocity makes this a difficult task. If a significant portion of the positive gradient region supported the same dominant wavelength, as the data suggest, this would be consistent with the concept of modeling the electrojet as a waveguide in which one dominant wave mode is launched (i.e., one with dimensions scaled to those of the waveguide, which in this case is the unstable region itself).

The Jicamarca radar data have shown that the large-scale horizontal waves are often observed to extend over several kilometers in altitude while maintaining the same phase. In one nighttime example [see *Farley et al.*, 1978, Figure 5] the large-scale waves show coherency over a range of 10–12 km, centered at 105 km.

Given the uncertainties of the measured in situ large-scale wave period, it is difficult to determine the manner in which the dominant wavelength varied in the lower electrojet. The rocket data do firmly establish, however, that the large-scale waves existed throughout the electrojet region where the ambient electron density gradient was unstable.

Amplitude and relationship of δE and $\delta n/n$. The linear relation between the electric field and plasma density perturbation amplitudes for long-wavelength waves is

$$\frac{\delta E}{E} = \frac{\nu_i}{\Omega_i} \frac{1}{(1+\psi)} \left[\frac{1+(ik_0/k)}{1+(k_0/k)^2}\right] \frac{\delta n}{n} \tag{8}$$

as given by *Kudeki* [1983]. For $k = k_0$, the modulus of (8) yields

$$\frac{\delta E}{E} = \frac{1}{2^{1/2}} \frac{\nu_i}{\Omega_i} \frac{1}{(1+\psi)} \frac{\delta n}{n} \tag{9}$$

Thus at 105 km, for $\delta E = E$, we would expect the plasma density fluctuation strength to be roughly 6.2%, in general agreement with the in situ measured values shown in Figure 8 (since k_{dominant} appears to be roughly equal to k_0 in this experiment).

Notice also from (8) that the appearance of an imaginary part implies a phase shift between δE and $\delta n/n$, given by

$$\phi = \tan^{-1}(k_0/k) \tag{10}$$

For $k = k_0$, $\phi = 45°$. From inspection of the time series data (Figure 8) a phase shift is not readily apparent between the δE and $\delta n/n$ waveforms, although this could easily have been masked by the fact that the lowest observed frequencies may represent, in actuality, a superposition of several modes. The phase relations are further distorted by the combination of the dispersion inherent in the long-wavelength waves given by (7) and the Doppler shift imposed by the vehicle motion, as discussed earlier.

Interaction of the large-scale waves with the polarization electric field. What ultimately limits the growth of the large-scale waves? The appearance of "squarelike" waveforms with sharp, steepened edges provides evidence that the large-scale, horizontal electric fields "saturate" in some manner. Furthermore, the fact that these steepened structures were observed on both the upleg and downleg only in the central region of the irregularity layer where the electrojet current was strongest implies that this saturation results from a nonlinear interaction between the plasma drifts of these waves and the ambient electrojet current. (The characteristics of the associated secondary two-stream waves driven in the upgoing and downgoing directions by these saturated horizontal wave electric fields are discussed in paper 3.)

Several theoretical papers discuss long-wavelength wave steepening and amplitude saturation effects inherent in the nonlinear evolution of gradient drift waves in the electrojet [e.g., *Sato*, 1971; *Rogister*, 1972; *Sudan et al.*, 1973; *Rognlien and Weinstock*, 1974; *Farley et al.*, 1978; *Kudeki et al.*, 1985; *Kawahara and Toh*, 1985], and many of these ideas appear to be supported by our measurements. Below, we discuss the nonlinear interaction of the kilometer scale waves with the electrojet current itself following the ideas of *Kudeki et al.* [1985], who predict a relationship between the maximum amplitudes of the waves and the polarization electric field, as well as explain a slight asymmetry in the east-west wave fields observed at Jicamarca.

As the long-wavelength instability grows, the oscillating horizontal electric fields create upward and downward plasma motions which enhance the depleted and enhanced plasma regions, respectively. As discussed by *Kudeki et al.* [1985], this action results in a net downward transport during the daytime. In order to satisfy $\nabla \cdot \mathbf{J} = 0$, however, a small induced electric field $\mathbf{E}_{\text{ind}}$ (directed downward during the day) will be set up to oppose further charge transfer by driving the plasma in the opposite direction. The drift due to $\mathbf{E}_{\text{ind}} \times \mathbf{B}$ will drive the electrojet current in the opposite way, opposing the normal electron drift. Thus the effect of the induced wave electric fields is to feed back and reduce the polarization field.

By balancing the Pedersen flux of the particles due to the wave action with the Hall current due to both the ambient and induced electric fields, the vertical wave velocity δv_z was shown by *Kudeki et al.* [1985] to achieve a maximum value such that

$$\delta v_z = \frac{1}{2^{1/2}} \mu_c E_0 = 2^{1/2} V_e \tag{11}$$

where μ_c is the Cowling mobility and E_0 is the ambient zero-order east-west electric field.

At 105 km, $\delta v_z/V_e = 1.44$, which implies that for a vertical electric field of 10 mV/m the largest value that the wave electric field can obtain would be 14.4 mV/m. The measured wave fields were between 10 and 15 mV/m, in reasonable agreement with this value, since we have estimated that the polarization field at 108 km was approximately 13.5 mV/m and decreased somewhat below this height where the large-scale waves were seen. Notice that the in situ data show that the waves had roughly the same electric field and plasma perturbation amplitudes (10–15 mV/m and 10%) throughout the entire electrojet region where the ambient electron density was unstable. This implies that the variation of wave amplitude with altitude does not follow that of the polarization electric field E_p, and suggests that nonlocal effects and other considerations are needed to account for the large wave amplitudes in the lower electrojet where the driving current is weak.

Whereas the rocket data did not provide a profile of the vertical polarization electric field, we can study the modulation of this parameter through the observations of the horizontal two-stream waves. For example, as shown in detail in paper 3, the primary two-stream waves vanished just below 106.5 km on the upleg precisely where the horizontal electric field direction switched from eastward to westward, indicating that at that location and time the instability threshold was no longer met. On the downleg at 105 km the phase of the large-scale wave was eastward, which corresponded exactly to where a very intense burst of two-stream wave activity occurred (see Figure 4*b*). These correlations provide evidence that the polarization (vertical) electric field (and hence the electrojet current) was modulated by the horizontal large-scale wave electric fields. In this manner, eastward fields augmented E_p, whereas westward fields diminished E_p. This relation is consistent with the interaction physics and asymmetry observations discussed by *Kudeki et al.* [1985]. However, whereas these authors averaged over an entire large-scale wavelength

to determine the net effect on the current, we comment below on these interaction processes using a more local approach.

In the absence of vertical currents, the simplest approximation for the establishment of the polarization electric field in the equatorial electrojet is given by

$$E_p = (-\sigma_2/\sigma_1)\, E_0 \tag{12}$$

where σ_1 and σ_2 are the Pedersen and Hall conductivities. (In this geometry, west and up are positive.) Then at 105 km an eastward electric field of 0.5 mV/m would produce a polarization field of about 15 mV/m directed upward. As mentioned above, the Jicamarca vertical radar has shown that the large-scale waves occur in phase over several kilometers [e.g., *Farley et al.*, 1978; *Kudeki et al.*, 1982; *Kudeki*, 1983]. Thus the plasma species must "see" the large-scale waves as "dc" fields over several kilometers in altitude. However, if we insert in (12) the observed values of the quasi-dc horizontal wave electric fields of 10–15 mV/m in place of the ambient east-west field, the new resulting polarization electric field would exceed 300 mV/m, which would be unrealistic and certainly detectable by our instruments. This reasoning further supports the view that the interaction physics limits and modulates the driving electric field as well as the horizontal wave amplitudes.

Notice in (12) that an eastward wave electric field in place of E_0 would enhance the ambient driving field while a westward wave electric field would decrease it, in exactly the same manner as inferred from the modulation of the observed two-stream waves discussed above. In the latter case (i.e., westward wave electric field), the net polarization field will probably still be directed upward (i.e., the electron current does not actually reverse) but may become so small that the threshold conditions for primary two-stream waves may locally not be met.

Since the gradient drift instability produces the large-scale waves in the first place and is itself driven by the horizontal electron drift, it is reasonable to assume that the modulated polarization electric field feeds back on the generation of the large-scale waves in such a manner as to increase the eastward field strengths during the daytime (with the opposite occurring at night). This would reinforce an asymmetry in the fields, as evidenced in the signature of two-stream secondaries observed by the Jicamarca vertical radar (see paper 1), eventually leading to a steady state balance of local currents, such as proposed by *Kudeki et al.* [1985].

Gradient Drift Spectra and Type 2 "Turbulence"

As discussed above, the largest-amplitude waves were shown to have wavelengths of a few kilometers and clearly dominated the irregularity spectrum. Notice in Figure 11, however, that the linear growth rate falls off for kilometer scale waves. Thus, in contrast to the two-stream case (shown in paper 3), the gradient drift spectrum apparently undergoes a substantial transfer of energy from the initially most unstable modes at wavelengths of several hundred meters to a fully developed peak at kilometer scale wavelengths. One plausible explanation for this fact, put forth by *Kudeki et al.* [1982], lies in the dispersive nature of the long-wavelength regime. Because these modes travel at different speeds, they do not exchange energy efficiently via a resonant mode coupling process and hence will grow until they are limited by other saturation effects.

In the intermediate-wavelength regime (30–300 m) the in situ observations and the computed unstable domains both show concentrated wave growth. Indications of organized waves at several hundred meters wavelength in the in situ spectra in the lower electrojet (see Figure 10) may indeed correspond to the most favorable regions of linear growth and may evolve differently than the large-scale waves excited above in the strongly interacting region where the current is strong. Alternatively, some of the observed peaks in the lower electrojet may correspond to the dominant nonlinear large-scale mode but with somewhat shorter wavelengths than those at 105 km.

Shorter time series spectra from this region indicate the presence of other seemingly random peaks embedded in the turbulence and suggest that the waves were arranged in groups of bursts which appeared organized by the large-scale wave electric fields. This microstructure implies that the probes encountered localized centers of intense growth, as is considered typical of turbulence. The generation of wave bursts related to the peaks of the electric field waveforms of the kilometer scale structures (see Figures 4*a* and 4*b*) is consistent with a two-step gradient drift process, such as that put forth by *Sudan et al.* [1973]. In this case, the large-scale wave electric fields may act in tandem with sharp density gradients of intermediate-scale waves, producing groups of "secondary" irregularities with scale lengths probably in the range of tens of meters, as discussed in paper 1. These waves could then generate shorter-scale waves via nonlinear turbulent processes such as mode coupling. The extension to relatively high rocket frame frequencies in some of the localized wave bursts may have been due, in part, to the generation of smaller scales but also may have resulted from the higher Doppler shifts that oblique and vertical waves would undergo because of the large vertical velocity component of the rocket's motion. This latter interpretation is consistent with our view that these bursts contain, at least partially, two-step secondary waves propagating normal to the local electric fields.

Despite the presence of two-step gradient drift waves and related "turbulence," the in situ spectra were observed to fall off at horizontal scale lengths of roughly 20–30 m, even when the spatial attenuation effects due to the double probe are taken into account. The linear growth rate calculations in Figure 11 using the ambient density profile show that wavelengths less than about 25 m will de damped in the lower electrojet. The in situ data thus imply that the turbulent mechanisms at work in this region could not produce enough secondary short-scale waves to fill out the spectrum at the level of the intermediate-scale waves, which we mainly associate with the first-order linearly unstable wavelength regime. Although some of the spectra representing shorter time series in the sonograms did show bursts extending to somewhat higher frequencies, the difficulties discussed earlier of parametrizing the contribution from nonhorizontal waves and determining their Doppler shifts preclude a more definitive interpretation of the in situ spectral forms. We can conclude from the observations of the inhomogeneity of the bursts, however, that whatever the nonlinear coupling processes were that might have been associated with these waves, they were damped on time scales short in comparison to the large-scale wave periods since a homogeneous, steady state turbulent spectrum did not result.

We know from the radar measurements, however, that 3-m waves with very small phase velocities existed throughout the lower electrojet, albeit with small backscatter power that decreased with decreasing altitudes. Traditionally, such observations have been used to argue that nonlinear plasma interac-

tions and turbulence must be at work in the gradient drift region to produce these very short scale irregularities that are otherwise linearly damped (see, for example, *Fejer and Kelley* [1980]). The meter scale waves observed by the radar during this experiment undoubtedly correspond to some of the oscillations recorded by the in situ probes. Although we cannot quantify such short scales in this instance, we can utilize the observed variation with altitude of the wave characteristics to shed light on the turbulent parameters necessary to generate these waves.

In general, the maximum frequency extent of the oscillations observed in situ declined somewhat with decreasing altitude between 100 and 90 km (see sonograms in Plate 1 and Figures 4*a* and 4*b*), implying that as $\mathbf{V}_d$ decreased and ψ increased, the maximum unstable wave number also decreased. Further, note that the variation of this damping scale length with altitude might have been masked in the data by any appreciable slowing of the waves at the lowest altitudes since they would have then been Doppler-shifted to higher frequencies in the rocket frame. Despite this uncertainty, the data suggest that the extent in k space of the gradient drift spectra weakened as a function of the background plasma parameters, which is consistent with theories that the electrojet turbulence extends to smaller scales via a mechanism that depends on the amount of free energy available [e.g., *Sudan*, 1983].

We can see this point in a different way by carrying the rocket and radar comparison one important step further. Although the radar began to detect vertical 3-m waves at roughly 94 km (see paper 1), the irregularity layer observed in situ extended down to about 90 km. We thus conclude that the in situ waveforms detected below 94 km represented waves with wavelengths longer than 3 m. This result supports the modeling of the gradient drift turbulence as a cascade process in which the shorter scales are fed from the strength of the intermediate (linearly unstable) turbulence, which then must compete with the local damping mechanisms. In other words, the combined in situ and radar data suggest that regardless of which mode-mode or other turbulent process was present to account for the 3-m vertical waves at 94 km and above, this mechanism was not strong enough to produce any vertical 3-m backscatter power below this altitude, despite the fact that longer-wavelength (intermediate-scale) irregularities were observed in this region by the rocket probes.

6. CONCLUSIONS

We have examined and discussed the overall characteristics of the irregularity layer observed in situ in the daytime equatorial electrojet including a detailed investigation of the waves generated by the gradient drift instability. The main conclusions of this section are as follows:

The Unstable Layer

1. The changing spectral characteristics of the observed irregularities depend critically on the local values of the current density, the gradient in the electron number density, and the parameter ψ.

2. The linear, fluid theory appears to do a reasonable job of predicting the altitude domain of the observed two-stream and gradient drift irregularities, based on the measured electron density and model current density profiles.

Large-Scale Waves

1. The observation of large-amplitude, long-wavelength waves solely on the upward gradient of the ambient daytime electron number density profile is consistent with a gradient drift explanation for their generation. The fact that the depletions and enhancements in electron density of the largest-scale modes were observed to correspond to upward and downward localized plasma drifts depicts the fundamental process inherent to the gradient drift instability.

2. The dominant large-scale wavelengths (roughly a few kilometers) observed by both the rocket probes and the radar appeared to correspond to k_0, a parameter dependent on the measured electron number density gradient defined such that $k_0 = v_t/\Omega_i(1 + \psi)L_N$. However, the actual parameters which determined the dominant mode may have included the effect of recombinations, the thickness of the layer, or a combination of all three factors.

3. The sharp, steepened edges and "flat-topped" or square waveforms of the east-west wave electric fields seen only in the region of strong electrojet current imply a saturation mechanism is in effect that may involve an interaction of the local plasma drifts and the ambient electron flow such that $\nabla \cdot \mathbf{J} = 0$.

Gradient Drift Spectrum

1. The largest observed amplitudes in the gradient drift spectrum occurred at wavelengths of several kilometers, much larger than the wavelength of maximum linear gradient drift growth. This suggests a substantial nonlinear transfer of energy to the dominant longest-wavelength modes.

2. The absence of a high-frequency component associated with the broad spectrum of intermediate-scale irregularities in the lower electrojet is consistent with the first-order damping of short-wavelength gradient drift modes.

3. The presence of "bursts" of short- and intermediate-scale waves associated with larger-amplitude, well-organized electric field structures in the gradient drift region suggests that a two-step gradient drift process was one mechanism that could explain their origin. Further, the data imply that on a scale of roughly 0.5 km the intermediate- and short-scale fluctuations do not represent a homogeneous layer, as is fairly typical of turbulence.

4. Below 94 km, where the Jicamarca radar did not observe any 3-m vertical backscatter power, the fact that the in situ probes still measured fluctuations implies that some intermediate-scale turbulence was present but that these waves were not strong enough to generate associated 3-m irregularities. This observation supports nonlinear turbulent cascade models in which the extent of the shortest wavelengths is governed by a growth/damping strength parameter [e.g., *Sudan*, 1983].

APPENDIX: DC ELECTRIC FIELD ANALYSIS USING THE SUM OF THE SQUARES TECHNIQUE

One technique for analyzing in situ double-probe measurements of electric fields in certain cases is to compute the square root of the sum of the squares of the two orthogonal spin plane components. This provides the spin plane component of $|\mathbf{E} + \mathbf{V} \times \mathbf{B}|$ from which the computed $|\mathbf{V} \times \mathbf{B}|$ contribution can then be subtracted. Although this procedure does not preserve the direction of $\mathbf{E}$ in the spin plane, this infor-

mation can be retrieved for horizontal spin plane measurements performed at the geomagnetic equator (such as was the case in this experiment) if the reasonable assumption that $\mathbf{E} \cdot \mathbf{B} = 0$ is made.

It is important to note that the above technique requires that $|\mathbf{V} \times \mathbf{B} + \mathbf{E}_0| \geq |\delta\mathbf{E}|$ where $\mathbf{E}_0$ is an essentially constant ambient field (in this case less than 1 mV/m) and $\delta\mathbf{E}$ represents the wave electric field. In other words, as discussed in detail by *Pfaff* [1986], if we consider the $\mathbf{V} \times \mathbf{B} + \mathbf{E}_0$ waveform to be the "carrier" signal modulated by $\delta\mathbf{E}$, this treatment will only be valid if "overmodulation" does not occur. This was indeed the case in the experiment described in this paper.

The dc electric field data shown in Figures 4*a*, 4*b*, 9, and 10 were computed in the manner described above. Because the irregularities were aligned in the plane perpendicular to the magnetic field and since the rocket axis was essentially vertical (within 10° of the magnetic zenith throughout the flight), the resulting spin plane quasi-dc fields could be interpreted in terms of horizontal components aligned in the east-west direction. As a check, the waveform polarities and amplitudes were compared to the solutions using the attitude (gyro) rotation matrix employed in the dc analysis described in regard to Figure 7 and were found to agree in both magnitude and phase.

A major advantage of the sum-of-the-squares technique is that since model sine waves do not need to be subtracted from each measured component, the residue at the spin frequency can be eliminated where the model fit is not exact. Further, power spectra of vector electric fields are more meaningful than those of single electric field components which contain large peaks at the spin frequency which in turn influence the amplitudes in the neighboring spectral bins.

Acknowledgments. We acknowledge useful discussions with D. T. Farley. We thank the staff of Jicamarca Observatory for providing the radar observations. Project Condor was a joint undertaking of the National Aeronautics and Space Administration (NASA) of the United States and of the Instituto Geofisico del Peru (IGP) and the Comision Nacional de Investigacions y Desarrollo Aerospacial (CONIDA) of Peru. We thank all of the personnel involved in the launch operations for their support and expertise in carrying out this experiment, and in particular, we acknowledge David Detwiler, the rocket payload manager at NASA/Wallops Flight Facility. The work at Cornell was sponsored by NASA under grant NSG-6020 and by the Division of Atmospheric Sciences of the National Science Foundation through grants ATM-8218619, ATM-8305500, and ATM-8418717.

The Editor thanks P. K. Chaturvedi and R. A. Greenwald for their assistance in evaluating this paper.

REFERENCES

Aikin, A. C., and L. J. Blumle, Rocket measurements of the *E* region electron concentration distribution in the vicinity of the geomagnetic equator, *J. Geophys. Res.*, *73*, 1617, 1968.

Baker, K. D., J. LaBelle, R. F. Pfaff, L. C. Howlett, N. B. Rao, J. C. Ulwick, and M. C. Kelley, Absolute electron density measurements in the equatorial ionosphere, *J. Atmos. Terr. Phys.*, *47*, 781, 1985.

Balsley, B. B., and D. T. Farley, Radar observations of two-dimensional turbulence in the equatorial electrojet, *J. Geophys. Res.*, *78*, 7471, 1973.

Balsley, B. B., B. G. Fejer, and D. T. Farley, Radar measurements of neutral winds and temperatures in the equatorial *E* region, *J. Geophys. Res.*, *81*, 1457, 1976.

Buneman, O., Excitation of field aligned sound waves by electron streams, *Phys. Rev. Lett.*, *10*, 285, 1963.

Farley, D. T., A plasma instability resulting in field-aligned irregularities in the ionosphere, *J. Geophys. Res.*, *68*, 6083, 1963.

Farley, D. T., The ionospheric plasma, in *Solar System Plasma Physics*, edited by C. F. Kennel, L. J. Lanzerotti, and E. N. Parker, North-Holland, Amsterdam, 1979.

Farley, D. T., Theory of equatorial electrojet plasma waves: New developments and current status, *J. Atmos. Terr. Phys.*, *47*, 729, 1985.

Farley, D. T., B. G. Fejer, and B. B. Balsley, Radar observations of two-dimensional turbulence in the equatorial electrojet, 3, Nighttime observations of type 1 waves, *J. Geophys. Res.*, *83*, 5625, 1978.

Fejer, B. G., and M. C. Kelley, Ionospheric irregularities, *Rev. Geophys.*, *18*, 401, 1980.

Fejer, B. G., D. T. Farley, B. B. Balsley, and R. F. Woodman, Vertical structure of the VHF backscattering region in the equatorial electrojet and the gradient drift instability, *J. Geophys. Res.*, *80*, 1313, 1975.

Forbes, J. M., The equatorial electrojet, *Rev. Geophys.*, *19*, 469, 1981.

Kawahara, T., and S. Toh, An approximate equation for nonlinear cross-field instability, *Phys. Lett. A*, *113*, 1, 1985.

Kudeki, E., Plasma turbulence in the equatorial electrojet, Ph.D. thesis, Cornell Univ., Ithaca, N. Y., 1983.

Kudeki, E., D. T. Farley, and B. G. Fejer, Long wavelength irregularities in the equatorial electrojet, *Geophys. Res. Lett.*, *9*, 684, 1982.

Kudeki, E., D. T. Farley, and B. G. Fejer, Theory of spectral asymmetries and nonlinear currents in the equatorial electrojet, *J. Geophys. Res.*, *90*, 429, 1985.

Kudeki, E., B. G. Fejer, D. T. Farley, and C. Hanuise, The Condor equatorial electrojet campaign: Radar results, *J. Geophys. Res.*, this issue.

Maeda, K., T. Tsunoda, and H. Maeda, Theoretical interpretation of the equatorial sporadic *E* layers, *Phys. Rev. Lett.*, *11*, 406, 1963.

Pfaff, R. F., Rocket studies of plasma turbulence in the equatorial and auroral electrojets, Ph.D. thesis, Cornell Univ., Ithaca, N. Y., 1986.

Pfaff, R. F., M. C. Kelley, B. G. Fejer, N. C. Maynard, and K. D. Baker, In-situ measurements of wave electric fields in the equatorial electrojet, *Geophys. Res. Lett.*, *9*, 688, 1982.

Pfaff, R. F., M. C. Kelley, B. G. Fejer, N. C. Maynard, L. H. Brace, B. G. Ledley, L. G. Smith, and R. F. Woodman, Comparative in-situ studies of the unstable day-time equatorial *E*-region, *J. Atmos. Terr. Phys.*, *47*, 791, 1985.

Pfaff, R. F., M. C. Kelley, E. Kudeki, B. G. Fejer, and K. D. Baker, Electric field and plasma density measurements in the strongly driven daytime equatorial electrojet, 2, Two-stream waves, *J. Geophys. Res.*, this issue.

Prakash, S., and S. Pal, Electric fields and electron density irregularities in the equatorial electrojet, *J. Atmos. Terr. Phys.*, *47*, 853, 1985.

Prakash, S., B. H. Subbaraya, and S. P. Gupta, Rocket measurements of ionization irregularities in the equatorial ionosphere at Thumba and identification of plasma irregularities, *Indian J. Radio Space Phys.*, *1*, 72, 1972.

Richmond, A. D., Equatorial electrojet, II, Use of the model to study the equatorial ionosphere, *J. Atmos. Terr. Phys.*, *35*, 1105, 1973.

Rogister, A., Nonlinear theory of cross-field instability with application to the equatorial electrojet, *J. Geophys. Res.*, *77*, 2975, 1972.

Rogister, A., and N. D'Angelo, Type 2 irregularities in the equatorial electrojet, *J. Geophys. Res.*, *75*, 3819, 1970.

Rognlien, T. D., and J. Weinstock, Theory of the nonlinear spectrum of the gradient drift instability in the equatorial electrojet, *J. Geophys. Res.*, *79*, 31, 1974.

Sampath, S., and T. S. G. Sastry, AC electric fields associated with the plasma instabilities in the equatorial electrojet, III, *J. Geomagn. Geoelectr.*, *31*, 391, 1979.

Sartiel, J., Champs électriques dans la région de l'électrojet équatorial, Ph.D. thesis, Univ. of Paris, VI, 1977.

Sato, T., Nonlinear theory of the cross-field instability—Explosive mode coupling, *Phys. Fluids*, *14*, 11, 1971.

Schmidt, M. J., and S. P. Gary, Density gradients and the Farley-Buneman instability, *J. Geophys. Res.*, *78*, 8261, 1973.

Simon, A., Instability of a partially ionized plasma in crossed electric and magnetic fields, *Phys. Fluids*, *6*, 382, 1963.

Smith, L. G., and O. Royrvik, Electron-density irregularities in the day-time equatorial ionosphere, *J. Atmos. Terr. Phys.*, *47*, 813, 1985.

Sudan, R. N., Unified theory of type I and type II irregularities in the equatorial electrojet, *J. Geophys. Res.*, *88*, 4853, 1983.

Sudan, R. N., J. Akinrimisi, and D. T. Farley, Generation of small-

scale irregularities in the equatorial electrojet, *J. Geophys. Res.*, *78*, 240, 1973.

K. D. Baker and B. G. Fejer, Center for Atmospheric and Space Sciences, Utah State University, Logan, UT 84322.

M. C. Kelley, School of Electrical Engineering, Cornell University, Ithaca, NY 14853.

E. Kudeki, Aeronomy Laboratory, University of Illinois, 1406 West Green Street, Urbana, IL 61801.

R. F. Pfaff, NASA Goddard Space Flight Center, Code 696, Greenbelt, MD 20771.

(Received March 25, 1987;
revised August 21, 1987;
accepted August 26, 1987.)